

An Iterative Newton–Raphson Method to Solve the Inverse Admittivity Problem

Peter M. Edic,* *Member, IEEE*, David Isaacson, *Member, IEEE*, Gary J. Saulnier, *Senior Member, IEEE*, Hemant Jain, and Jonathan C. Newell, *Member, IEEE*

Abstract—By applying electrical currents to the exterior of a body using electrodes and measuring the voltages developed on these electrodes, it is possible to reconstruct the electrical properties inside the body. This technique is known as electrical impedance tomography. The problem is nonlinear and ill conditioned meaning that a large perturbation in the electrical properties far away from the electrodes produces a small voltage change on the boundary of the body.

This paper describes an iterative reconstruction algorithm that yields approximate solutions of the inverse admittivity problem in two dimensions. By performing multiple iterations, errors in the conductivity and permittivity reconstructions that result from a linearized solution to the problem are decreased. A finite-element forward-solver, which predicts voltages on the boundary of the body given knowledge of the applied current on the boundary and the electrical properties within the body, is required at each step of the reconstruction algorithm. Reconstructions generated from numerical data are presented that demonstrate the capabilities of this algorithm.

Index Terms—Conductivity, impedance imaging, iterative reconstruction methods, least-squares reconstruction methods, permittivity.

I. INTRODUCTION

ELECTRICAL properties of a patient or object may be computed from electrical measurements made on the surface of the body using a technology known as electrical impedance tomography (EIT). Ideally, the voltage on the boundary of the object is measured while a current density is applied to its surface. The mathematical model that describes the system is [1]

$$\nabla \cdot \tilde{\sigma}(p) \nabla \tilde{U}(p) = 0 \quad \text{in } B \quad (1)$$

$$\tilde{\sigma}(p) \frac{\partial \tilde{U}(p)|_{p \in S}}{\partial \nu} = j, \quad \text{on } S \quad (2)$$

$$\int \tilde{U}(p)|_{p \in S} dS = 0 \quad (3)$$

where

Manuscript received August 27, 1996; revised February 2, 1998. Asterisk indicates corresponding author.

*P. M. Edic is with the General Electric Corporate Research and Development, Schenectady, NY, 12309 USA (e-mail: edic@crd.ge.com).

D. Isaacson is with the Department of Mathematical Sciences, Rensselaer Polytechnic Institute, Troy, NY 12180 USA.

G. J. Saulnier is with the Department of Electrical, Computer, and Systems Engineering, Rensselaer Polytechnic Institute, Troy, NY 12180 USA.

H. Jain is with Epic Systems Corporation, Madison, WI 53711 USA.

J. C. Newell is with the Department of Biomedical Engineering, Rensselaer Polytechnic Institute, Troy, NY 12180 USA.

Publisher Item Identifier S 0018-9294(98)04445-0.

B denotes the body of the object, while S denotes the surface of the object;

$\tilde{U}(p)$ complex potential distribution in B and on S ;

$\tilde{\sigma}(p)$ admittivity of B . It is defined as $\sigma(p) + i\omega\epsilon(p)$, where σ is the electrical conductivity, ω is the angular frequency of the applied current waveform, and ϵ is the electrical permittivity;

j current density applied on S ;

ν outward normal of B defined on S .

In the text that follows, $\{\cdot\}$ is used to denote that $\{\cdot\}$ is a complex quantity.

Equation (1) specifies that no source resides in the body and that charge is not allowed to accumulate in the body. Equation (2) constrains the current entering B to be the integral of the applied current density. Equation (3) is necessary for the existence of a unique solution to the system model.

With knowledge of all current densities applied on S and the voltages measured on S , $\tilde{\sigma}(p)$ can be determined for all positions p in the body [2]. However, in practice, currents are applied and voltages measured on S at discrete regions using electrodes. Since a finite number of voltage measurements are recorded, it is possible to determine the admittivity distribution using a finite number of degrees of freedom. For a system with L electrodes, $N = (L(L-1))/2$ degrees of freedom can be computed [1] for the admittivity distribution. The number of degrees of freedom can be distributed as piecewise-constant regions in the domain or multiplicative constants of basis functions that exist over the entire region B .

Several reconstruction techniques have been used to compute the electrical properties within the region B . Of particular interest are filtered backprojection and least-squares techniques. In practice, the filtered backprojection technique projects a voltage difference signal, produced from measurements on the boundary of the body made under two different sets of conditions, along isopotential lines in the body [3]–[5]. This technique has been used mostly to generate dynamic images of the body and display the effects of a change in the electrical properties of the body at two specific conditions.

In the least-squares method, an objective function is selected, and the residuals of this function are minimized [1], [6]–[11]. Iterative approaches used to minimize the objective function are presented in [8] and [9]; these papers consider only the conductivity problem and do not discuss the *admittivity* problem.

An important topic in EIT is the notion of distinguishability. This quantity is used to characterize the ability of a reconstruction algorithm in distinguishing two separate admittivity

distributions. Although this topic is not discussed here, [12] and [13] report on this topic for the inverse conductivity problem.

This paper describes an iterative method to solve the admittivity problem. Better estimates of the true permittivity and conductivity distributions are reconstructed when complex voltage data on S are used as input to the reconstruction algorithm. Reconstructions of numerical data are presented that demonstrate this effect.

II. DESCRIPTION OF THE ALGORITHM

An earlier reconstruction algorithm known as Newton's one-step error reconstructor (NOSER), developed in [1], uses one step of a Newton-Raphson method to solve a nonlinear system of equations that results from the minimization of an error functional involving voltages measured on S and those predicted from a forward-solver. The forward-solver used in that algorithm predicts the boundary voltages given knowledge of either the conductivity or permittivity distribution in B and the current waveforms applied to S .

The present complex Newton's recursive-step error reconstructor (CNRSER) algorithm performs multiple steps of the Newton-Raphson method in solving a nonlinear system of equations, resulting from an error expression that is similar to that used in the NOSER algorithm. However, the CNRSER algorithm *iteratively* solves the *full* complex problem, overcoming two limitations of NOSER which implements only *one* step of the Newton-Raphson method to solve either the inverse conductivity or permittivity problem *separately*. Yorkey *et al.* demonstrated that the iterative Newton-Raphson method is desirable since it converges to the smallest error between measured and predicted voltages in the fewest iterations of the methods tested [10].

A. One Step of the CNRSER Algorithm

In the CNRSER algorithm, the admittivity distribution consists of N piecewise-constant regions and is defined as

$$\vec{\sigma} = \sum_{n=1}^N (\sigma_n + i\omega\epsilon_n) \chi_n = \vec{\sigma} + i\omega\vec{\epsilon} \quad (4)$$

where χ_n is unity on the n th mesh element and zero everywhere else. Fig. 1 shows a picture of the mesh elements used in the CNRSER algorithm, denoted as the Joshua Tree Mesh. It is possible to define another quantity $\vec{\rho}$ which is the reciprocal of $\vec{\sigma}$, called the impedivity, and is defined as

$$\vec{\rho} = \sum_{n=1}^N (\rho_n + i q_n) \chi_n = \vec{\rho} + i \vec{q} \quad (5)$$

where

$$\rho_n = \frac{\sigma_n}{\sigma_n^2 + (\omega\epsilon_n)^2} \quad (6)$$

and

$$q_n = \frac{-\omega\epsilon_n}{\sigma_n^2 + (\omega\epsilon_n)^2}. \quad (7)$$

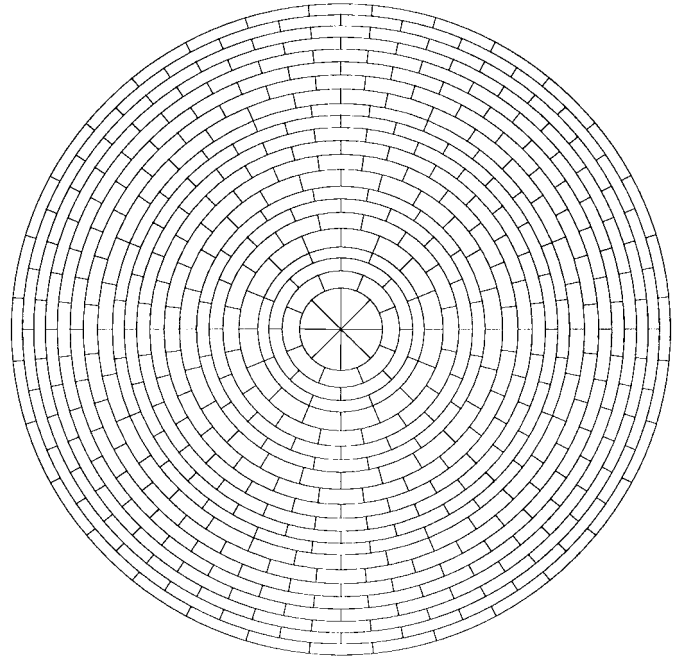


Fig. 1. The Joshua Tree Mesh used in the CNRSER algorithm.

The following error functional is used in the iterative reconstruction algorithm:

$$\delta(\vec{\rho}) = \underbrace{\sum_{k=1}^{L-1} \sum_{l=1}^L \left\{ \tilde{U}_l^k(\vec{\rho}) - \tilde{V}_l^k \right\} \left\{ \tilde{U}_l^k(\vec{\rho}) - \tilde{V}_l^k \right\}^*}_{\alpha} + \underbrace{\Gamma \int_B \nabla \vec{\rho} \cdot (\nabla \vec{\rho})^* dB}_{\beta} \quad (8)$$

where

- l number of the electrode on S , $l = 1, \dots, L$;
- k number of the current pattern applied on S to all L electrodes simultaneously, $k = 1, \dots, L-1$;
- $\tilde{U}_l^k(\vec{\rho})$ forward-solver voltage predicted on the l th electrode given that the k th current pattern was applied on S and that $\vec{\rho}$ characterizes the electrical properties of B ;
- \tilde{V}_l^k experimental voltage measured on the l th electrode when the k th current pattern was applied;
- α error functional used in the NOSER algorithm;
- β gradient regularization term that forces the reconstruction to be spatially smooth by penalizing the error functional by the squared-magnitude of the gradient of the impedivity distribution;
- Γ gain factor applied to the regularization term;
- $\{\cdot\}^*$ denotes the complex conjugate of $\{\cdot\}$.

In particular, $\tilde{U}_l^k(\vec{\rho})$ denotes the complex, forward-solver voltage that results from the application of the k th current pattern of the canonical set, shown in (9) at the bottom of the next page.

The error functional can be rewritten in terms of real quantities as

$$\begin{aligned} \delta(\vec{\rho}) = & \sum_{k=1}^{L-1} \sum_{l=1}^L \left\{ U_{r,l}^k(\vec{\rho}) - V_{r,l}^k \right\}^2 \\ & + \sum_{k=1}^{L-1} \sum_{l=1}^L \left\{ U_{q,l}^k(\vec{\rho}) - V_{q,l}^k \right\}^2 \\ & + \Gamma \int_B \nabla \vec{\rho} \cdot \nabla \vec{\rho} dB + \Gamma \int_B \nabla \vec{q} \cdot \nabla \vec{q} dB \end{aligned} \quad (10)$$

where $\{\cdot\}_{r,l}^k$ denotes the real part of $\{\cdot\}_l^k$ and $\{\cdot\}_{q,l}^k$ denotes the imaginary part of $\{\cdot\}_l^k$.

The goal of the reconstruction algorithm is to find ρ_n and q_n for $n = 1, \dots, N$ that minimize this error functional. A standard method [14], [15] for minimizing (10) is to let

$$\begin{aligned} F_{\rho_n} = & \frac{\partial \delta(\vec{\rho})}{\partial \rho_n} = 2 \sum_{k=1}^{L-1} \sum_{l=1}^L \left\{ U_{r,l}^k(\vec{\rho}) - V_{r,l}^k \right\} \frac{\partial U_{r,l}^k(\vec{\rho})}{\partial \rho_n} \\ & + 2 \sum_{k=1}^{L-1} \sum_{l=1}^L \left\{ U_{q,l}^k(\vec{\rho}) - V_{q,l}^k \right\} \frac{\partial U_{q,l}^k(\vec{\rho})}{\partial \rho_n} \\ & + 2\Gamma \int_B \nabla \frac{\partial \vec{\rho}}{\partial \rho_n} \cdot \nabla \vec{\rho} dB = 0 \end{aligned} \quad (11)$$

$$\begin{aligned} F_{q_n} = & \frac{\partial \delta(\vec{\rho})}{\partial q_n} = 2 \sum_{k=1}^{L-1} \sum_{l=1}^L \left\{ U_{r,l}^k(\vec{\rho}) - V_{r,l}^k \right\} \frac{\partial U_{r,l}^k(\vec{\rho})}{\partial q_n} \\ & + 2 \sum_{k=1}^{L-1} \sum_{l=1}^L \left\{ U_{q,l}^k(\vec{\rho}) - V_{q,l}^k \right\} \frac{\partial U_{q,l}^k(\vec{\rho})}{\partial q_n} \\ & + 2\Gamma \int_B \nabla \frac{\partial \vec{q}}{\partial q_n} \cdot \nabla \vec{q} dB = 0 \end{aligned} \quad (12)$$

and solve the vector equation

$$\vec{F} = [F_{\rho_1} \ F_{\rho_2} \ \dots \ F_{\rho_N} \ F_{q_1} \ F_{q_2} \ \dots \ F_{q_N}]^T = 0 \quad (13)$$

by a Newton-Raphson method. We define

$$\vec{\eta} = [\rho_1 \ \rho_2 \ \dots \ \rho_N \ q_1 \ q_2 \ \dots \ q_N]^T \quad (14)$$

and use this method

$$\vec{\eta}_{s+1} = \vec{\eta}_s - J_s^{-1} \vec{F}_s \quad (15)$$

to iteratively compute the solution to this nonlinear system of $2N$ equations. Here, J is the Jacobian of \vec{F}

$$J = \begin{bmatrix} \frac{\partial F_{\rho_1}}{\partial \rho_1} & \dots & \frac{\partial F_{\rho_1}}{\partial \rho_N} & \frac{\partial F_{\rho_1}}{\partial q_1} & \dots & \frac{\partial F_{\rho_1}}{\partial q_N} \\ \frac{\partial F_{\rho_2}}{\partial \rho_1} & \dots & \frac{\partial F_{\rho_2}}{\partial \rho_N} & \frac{\partial F_{\rho_2}}{\partial q_1} & \dots & \frac{\partial F_{\rho_2}}{\partial q_N} \\ \vdots & \vdots & \vdots & \vdots & \vdots & \vdots \\ \frac{\partial F_{q_1}}{\partial \rho_1} & \dots & \frac{\partial F_{q_1}}{\partial \rho_N} & \frac{\partial F_{q_1}}{\partial q_1} & \dots & \frac{\partial F_{q_1}}{\partial q_N} \\ \vdots & \vdots & \vdots & \vdots & \vdots & \vdots \\ \frac{\partial F_{q_N}}{\partial \rho_1} & \dots & \frac{\partial F_{q_N}}{\partial \rho_N} & \frac{\partial F_{q_N}}{\partial q_1} & \dots & \frac{\partial F_{q_N}}{\partial q_N} \end{bmatrix}. \quad (16)$$

Four separate expressions for the components of J are given in the Appendix. Although the second-order partial derivatives of the potential terms in these expressions affect algorithm convergence, they are difficult to compute. However, after a few iterations, the difference between the predicted voltages and the measured voltages, the factor multiplying these terms, will be small. For this reason, these terms are not computed and simply neglected in the reconstruction algorithm. Likewise, the second-order partial derivatives of the real and quadrature components of the impedivity vanish with a suitable choice of basis functions for these two quantities (discussed later).

As described in [1] and [10], Marquardt regularization is a useful technique to improve the conditioning of the Jacobian matrix used in solving the inverse admittivity problem. However, after several steps of the CNRSER algorithm, the computed impedivity distribution becomes very peaked using this regularization method for certain impedivity distributions. The gradient regularization term, the β expression in (8), forces the reconstructed impedivity distribution to be spatially smooth at the expense of increased error between measured and predicted voltages on S .

The orthonormal canonical current patterns specified in (9) are denoted by $\{T^\tau: \tau = 1, \dots, L-1\}$. Neglecting second-order partial derivatives, the expressions defined in the Appendix can be written as

$$\begin{aligned} \frac{\partial F_{\rho_n}}{\partial \rho_m} = & 2 \sum_{k=1}^{L-1} \sum_{\tau=1}^{L-1} R_{r,\rho_n}^{k,\tau}(\vec{\rho}) R_{r,\rho_m}^{k,\tau}(\vec{\rho}) \\ & + 2 \sum_{k=1}^{L-1} \sum_{\tau=1}^{L-1} R_{q,\rho_n}^{k,\tau}(\vec{\rho}) R_{q,\rho_m}^{k,\tau}(\vec{\rho}) \\ & + 2\Gamma \int_B \nabla \frac{\partial \vec{\rho}}{\partial \rho_n} \cdot \nabla \frac{\partial \vec{\rho}}{\partial \rho_m} dB \end{aligned} \quad (17)$$

$$\begin{aligned} \frac{\partial F_{q_n}}{\partial \rho_m} = & 2 \sum_{k=1}^{L-1} \sum_{\tau=1}^{L-1} R_{r,q_n}^{k,\tau}(\vec{\rho}) R_{r,\rho_m}^{k,\tau}(\vec{\rho}) \\ & + 2 \sum_{k=1}^{L-1} \sum_{\tau=1}^{L-1} R_{q,q_n}^{k,\tau}(\vec{\rho}) R_{q,\rho_m}^{k,\tau}(\vec{\rho}) \end{aligned} \quad (18)$$

$$\frac{\partial F_{\rho_n}}{\partial q_m} = \frac{\partial F_{q_m}}{\partial \rho_n} \quad (19)$$

$$I_l^k = \begin{cases} \sqrt{\frac{2}{L}} \cos\left(\frac{2\pi}{L} kl\right) & k = 1, \dots, \frac{L}{2} - 1; l = 1, \dots, L \\ \sqrt{\frac{1}{L}} \cos(\pi l) & k = \frac{L}{2}; l = 1, \dots, L \\ \sqrt{\frac{2}{L}} \sin\left[\frac{2\pi}{L} k\left(l - \frac{L}{2}\right)\right] & k = \frac{L}{2} + 1, \dots, L - 1; l = 1, \dots, L \end{cases} \quad (9)$$

$$\begin{aligned}
\frac{\partial F_{q_n}}{\partial q_m} = & 2 \sum_{k=1}^{L-1} \sum_{\tau=1}^{L-1} R_{r,q_n}^{k,\tau}(\vec{\rho}) R_{r,q_m}^{k,\tau}(\vec{\rho}) \\
& + 2 \sum_{k=1}^{L-1} \sum_{\tau=1}^{L-1} R_{q,q_n}^{k,\tau}(\vec{\rho}) R_{q,q_m}^{k,\tau}(\vec{\rho}) \\
& + 2\Gamma \int_B \nabla \frac{\partial \vec{q}}{\partial q_n} \cdot \nabla \frac{\partial \vec{q}}{\partial q_m} dB
\end{aligned} \quad (20)$$

where

$$R_{r,\rho_n}^{k,\tau}(\vec{\rho}) \equiv \left\langle \frac{\partial U_r^k(\vec{\rho})}{\partial \rho_n}, T^\tau \right\rangle \quad (21)$$

and $\langle a, b \rangle$ is defined as the vector inner product of vectors a and b . The remaining terms in these equations can be inferred from the definition in (21). Using the complex equivalent of a result derived in [1], one can show that

$$\begin{aligned}
R_{r,\rho_n}^{k,\tau} \approx & \frac{\partial \sigma}{\partial \rho_n} \int_{\chi_n} \left(\nabla U_r^k \cdot \nabla U_r^\tau - \nabla U_q^k \cdot \nabla U_q^\tau \right) dB \\
& - \frac{\partial \omega \epsilon}{\partial \rho_n} \int_{\chi_n} \left(\nabla U_r^k \cdot \nabla U_q^\tau - \nabla U_q^k \cdot \nabla U_r^\tau \right) dB
\end{aligned} \quad (22)$$

$$\begin{aligned}
R_{q,\rho_n}^{k,\tau} \approx & \frac{\partial \omega \epsilon}{\partial \rho_n} \int_{\chi_n} \left(\nabla U_r^k \cdot \nabla U_r^\tau - \nabla U_q^k \cdot \nabla U_q^\tau \right) dB \\
& + \frac{\partial \sigma}{\partial \rho_n} \int_{\chi_n} \left(\nabla U_r^k \cdot \nabla U_q^\tau - \nabla U_q^k \cdot \nabla U_r^\tau \right) dB
\end{aligned} \quad (23)$$

$$R_{q,q_n}^{k,\tau} = R_{r,\rho_n}^{k,\tau} \quad (24)$$

$$R_{r,q_n}^{k,\tau} = -R_{q,\rho_n}^{k,\tau} \quad (25)$$

where the dependence on $\vec{\rho}$ has been omitted for simplicity. The integral is computed over the area enclosed by the piecewise-constant mesh element, denoted as χ_n .

Since the impedivity distribution is piecewise-constant, the gradient of this distribution is zero in the area enclosed by the mesh elements and infinity at the edges of the mesh elements. To approximate the gradient, the center-point of each mesh element was computed and a basis function ϕ_n was constructed that linearly interpolated in the radial and angular directions between adjacent mesh element centers. Fig. 2 shows a typical basis function; it has an amplitude of 1.0 at the center of the mesh element of interest and linearly interpolates to 0.0 at the boundaries of the basis function. The gradient of the impedivity distribution is then approximated by computing the gradient of

$$\vec{\rho} \approx \sum_{n=1}^N (\rho_n + i q_n) \phi_n = \vec{\rho} + i \vec{q}. \quad (26)$$

The gradients of $\vec{\rho}$ and \vec{q} are

$$\nabla \vec{\rho} = \sum_{n=1}^N \rho_n \nabla \phi_n \quad (27)$$

$$\nabla \vec{q} = \sum_{n=1}^N q_n \nabla \phi_n \quad (28)$$

where ϕ_n , $n = 1, \dots, N$, is a basis function typical of the one shown in Fig. 2. The partial derivatives of $\nabla \vec{\rho}$ and $\nabla \vec{q}$

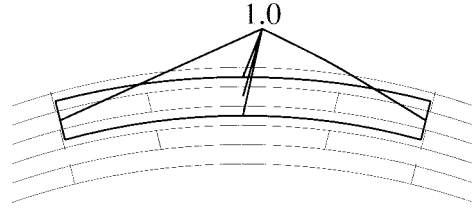


Fig. 2. Basis functions used to develop an approximation to the piecewise constant impedivity distribution.

with respect to ρ_n and q_n are also computed using these expressions.

The gain factor Γ in (8) is chosen so the root-mean-squared (rms) error between measured and predicted voltages is comparable to the measurement precision of the tomograph. Hence, the value Γ can be iteratively chosen to satisfy this constraint.

B. Multiple Steps of the CNRSER Algorithm

The quantities defined in the previous section must be computed at each iteration of the CNRSER algorithm. For the first step of the CNRSER algorithm, the conductivity and permittivity distributions are chosen to be constant. A guess is made at these values by minimizing (10) with respect to two constants: one representing the real part of the homogeneous impedivity and one representing the imaginary part of the homogeneous impedivity.

To compute the quantities in (15), a forward-solver that uses the piecewise-constant admittivity distribution must be employed at each step. A finite-element forward solution is used for this purpose. Each element of the Joshua Tree Mesh, shown in Fig. 1, is segmented into several triangles. The triangulation of the Joshua Tree Mesh is used by the forward-solver to compute voltages at each node in B and on S . (A node refers to a vertex of a triangle in the mesh.) These data are then used to compute \vec{F} and J at each iteration. The CNRSER algorithm computes a new estimate of $\vec{\rho}$, which is used by the forward-solver to generate the predicted voltages. The process continues until the reconstruction converges to its final result.

III. METHODS

The CNRSER algorithm was tested using numerical data. The Joshua Tree Mesh was segmented into 9216 triangles for the finite-element forward-solver algorithm.

The electrode model used to generate the voltage data sets was the *gap* model [1]. In this model, the current in each electrode is specified by (9) and the current density is assumed to be constant over the electrode region. The current density in *gap* regions between electrodes is assumed to be zero. In [16], [17], and [18], more accurate models for the electrodes are specified. Although these models will yield better reconstructions of experimental data, they are not incorporated in our model since the reconstruction algorithm presented here assumes the *gap* model for the electrodes. In this manner, electrode modeling errors will not corrupt the results to be presented.

To determine the precision of the forward-solver, a model of a circular phantom consisting of a homogeneous conductivity

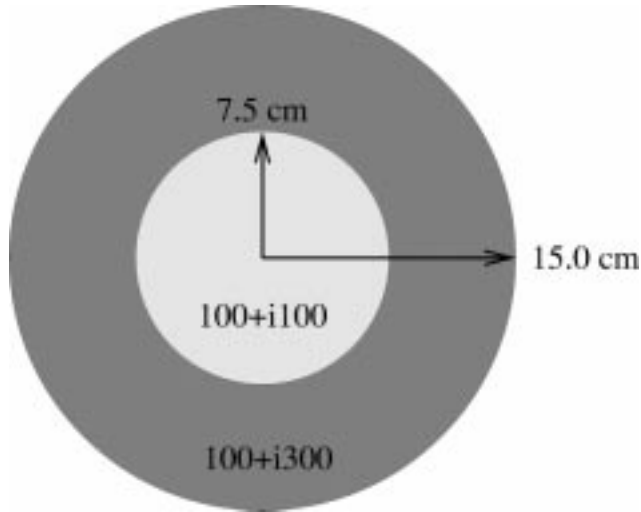


Fig. 3. Admittivity distribution consisting of a homogeneous conductivity distribution and a permittivity distribution with a step inhomogeneity. (Units are millisiemens per meter.)

was developed. Both the finite-element forward-solver and an analytical expression were used to compute boundary voltages on S when the current patterns specified in (9) were applied to the electrodes. Using the voltages calculated with the analytical model as the true values, the maximum error in voltages predicted on S by the finite-element forward-solver was 0.12% of the maximum voltage amplitude that was computed.

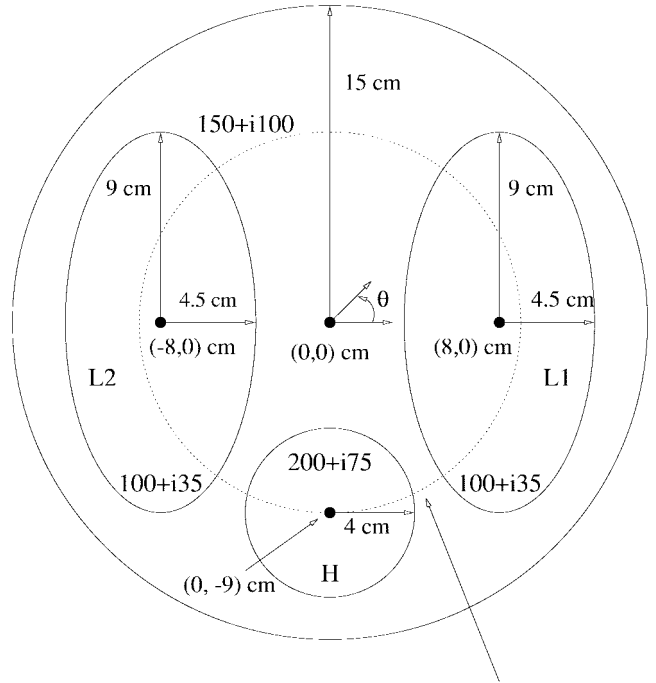
The real component of admittivity is conductivity while the imaginary component is permittivity scaled by the angular frequency of the applied current waveform. However, in the text that follows, the imaginary part of the admittivity is simply denoted as the permittivity. This nomenclature will make discussions more readable as well as allow direct comparison of magnitudes of both the real and imaginary components of the admittivity.

A. Numerical Voltage Data Generated from an Analytical Model

Given the current density on the boundary of the Joshua Tree Mesh, one can write the Fourier series for the current density applied on S since this function is periodic in angular position. For the analytical model, the conductivity distribution is circularly symmetric with a centered inhomogeneity, as shown in Fig. 3. The admittivity distribution is homogeneous in conductivity (100 mS/m) and has a step inhomogeneity in permittivity (200 mS/m) at a radius equaling 0.5 of the total radius of the object.

The equation for the boundary voltage is developed by solving the boundary-value problem using Laplace's Equation in each homogeneous region in Fig. 3. This solution was used to generate complex voltage data that were used as input to the CNRSER algorithm. A figure-of-merit for determining the benefit of the iterative solution will be the reduction in the squared error of the difference between measured voltages and those predicted by the forward-solver.

The real and quadrature voltage files were also used *separately* as inputs to the reconstruction algorithm. Reconstructions of these data will be compared to the reconstructions



Path of Circular Cross-section

Fig. 4. Admittivity distribution simulating a cross section of a human chest containing lungs and a heart. (Admittivity units are millisiemens per meter.)

computed using complex voltage data to demonstrate the benefits of the CNRSER algorithm.

For all reconstructions, Marquardt regularization (gain equal to 0.01) was applied to the Jacobian matrix. The gain (Γ) of the gradient regularization term in (8) was chosen to be zero.

B. Numerical Voltage Data Generated from a Simulated Human Chest

Fig. 4 shows a cross section of the phantom used to simulate a human chest. Two regions are included which simulate human lungs as well as a region that simulates a human heart. Reasonable admittivity values for the objects in the phantom were based on experimental data collected from living tissue as reported in [19]. In particular, the admittivity of the lungs is $100 + i35$ mS/m, the admittivity of the heart is $200 + i75$ mS/m, and the admittivity of the remaining portion of the phantom is $150 + i100$ mS/m, the value typical of muscle tissue.

A boundary-element forward-solver was used to generate the boundary voltage data for this geometry. This algorithm used the *gap* model for electrode regions, which is compatible with the reconstruction algorithm. Suitable noise from a uniform deviate was added to the data to simulate a voltmeter precision of 1 part in 4096 (12 bits). The voltage data corrupted with noise were used as input to the CNRSER algorithm to generate a reconstruction of the phantom. Reconstructions of the real and quadrature voltage data were also computed separately to demonstrate the benefits of the CNRSER algorithm and the reconstruction errors that occur if the real and quadrature components of the voltages measured on S are considered separately. For all reconstructions, Marquardt regularization (gain equal to 0.2) was applied to the Jacobian matrix; the gain (Γ) of the gradient regularization term in (8) was chosen to be zero.

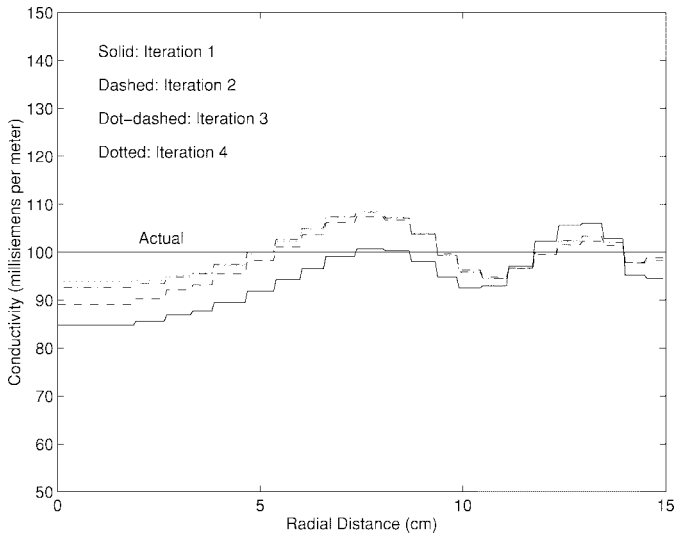


Fig. 5. Conductivity distributions as a function of the radial distance from the center of the Joshua Tree Mesh, calculated after each of four iterations of the CNRSER algorithm using complex voltage data generated from the geometry in Fig. 3.

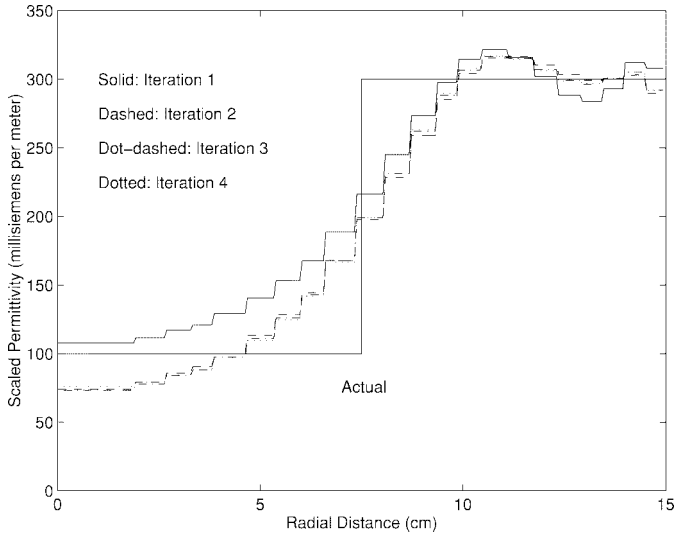


Fig. 6. Permittivity distributions as a function of the radial distance from the center of the Joshua Tree Mesh, calculated after each of four iterations of the CNRSER algorithm using complex voltage data generated from the geometry in Fig. 3.

Reconstructions of the complex voltage data corrupted with noise were computed using gradient regularization (gain equal to 1.0) to demonstrate the benefits of this technique. When using experimental data with the CNRSER algorithm, Γ should be selected so that the rms value of the residual error in (8) is comparable to system noise in the tomograph.

IV. RESULTS

A. Output of the CNRSER Algorithm Using the Analytical Model

Since the admittivity distribution shown in Fig. 3 is circularly symmetric, the output of the CNRSER algorithm is also circularly symmetric; hence, radial cross sections of the reconstructed conductivity and permittivity distributions are

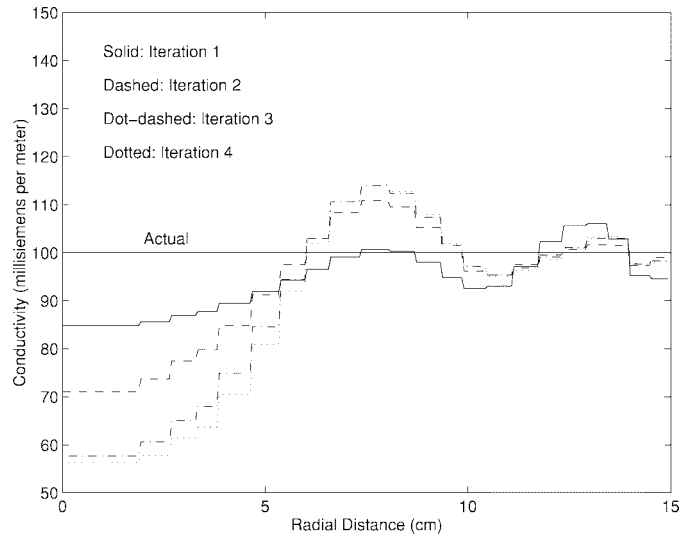


Fig. 7. Conductivity distributions as a function of the radial distance from the center of the Joshua Tree Mesh, calculated after each of four iterations of the CNRSER algorithm using separate real and quadrature voltage data generated from the geometry in Fig. 3.

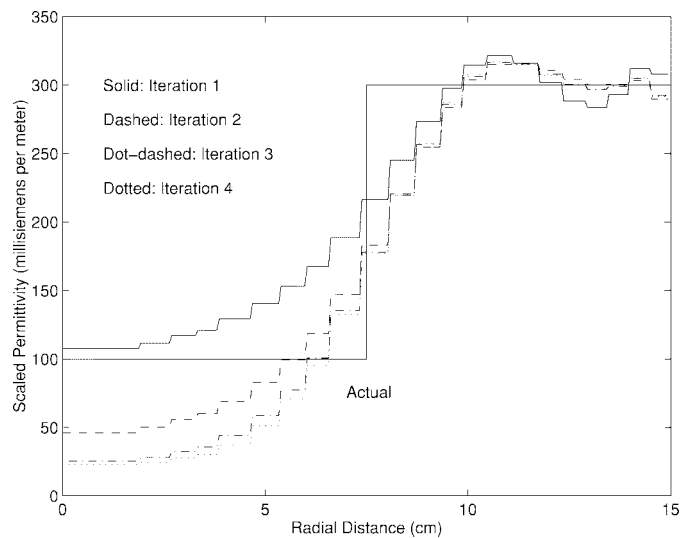


Fig. 8. Permittivity distributions as a function of the radial distance from the center of the Joshua Tree Mesh, calculated after each of four iterations of the CNRSER algorithm using separate real and quadrature voltage data generated from the geometry in Fig. 3.

used to display the output of the algorithm. Figs. 5 and 6 show the reconstructed conductivity and permittivity distributions, respectively, after several iterations of the CNRSER algorithm as a function of the radial distance from the center of the admittivity distribution shown in Fig. 3. The squared error between measured and predicted voltages decreased by a factor of 2.05×10^5 after four iterations.

Figs. 7 and 8 show cross sections of the reconstructed conductivity and permittivity distributions, respectively, when the real and quadrature voltage files were used separately as input to the reconstruction algorithm. For this case, the squared-error between the real components of the measured and predicted voltages decreased by a factor of 7.15×10^2 after four iterations while the squared error between the imaginary components of the measured and predicted voltages decreased by a factor of 1.59×10^5 .

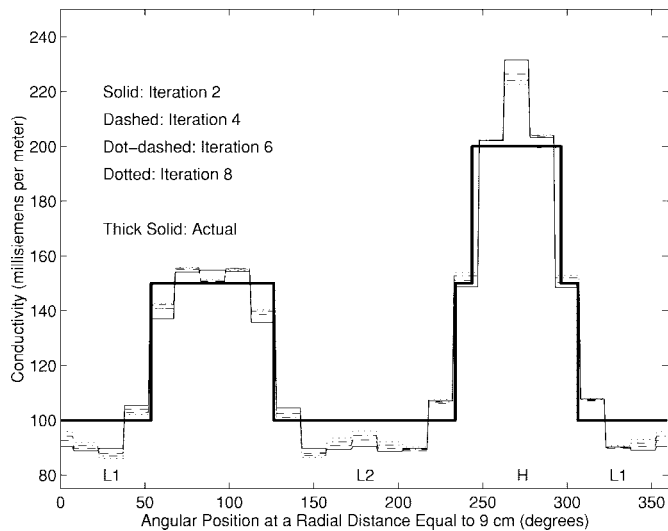


Fig. 9. Conductivity distribution as a function of angular position, calculated after several iterations of the CNRSER algorithm using complex voltage data generated from the geometry in Fig. 4. Marquardt regularization of the Jacobian matrix was implemented for these reconstructions.

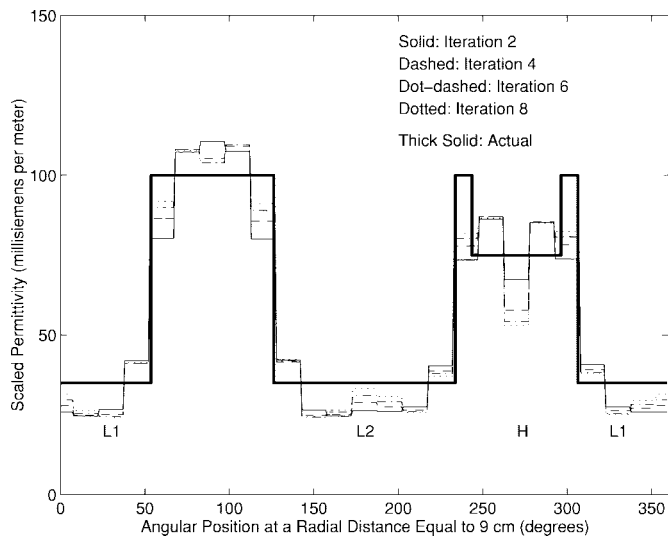


Fig. 10. Permittivity distribution as a function of angular position, calculated after several iterations of the CNRSER algorithm using complex voltage data generated from the geometry in Fig. 4. Marquardt regularization of the Jacobian matrix was implemented for these reconstructions.

It is important to note that the reconstruction algorithm could not exactly reconstruct the true distribution since the boundary of the centered inhomogeneity was purposely chosen so as not to coincide with a boundary of the Joshua Tree Mesh.

B. Output of the CNRSER Algorithm Using Voltage Data from a Simulated Human Chest

Figs. 9 and 10 show the conductivity and permittivity distribution, respectively, computed by the CNRSER algorithm, using the model shown in Fig. 4. The squared error between measured and predicted voltages decreased by a factor of 2.44×10^3 after eight iterations. Figs. 11 and 12 show the conductivity and permittivity distribution, respectively, computed by the CNRSER algorithm when the real and quadrature voltage data were used as separate input to the

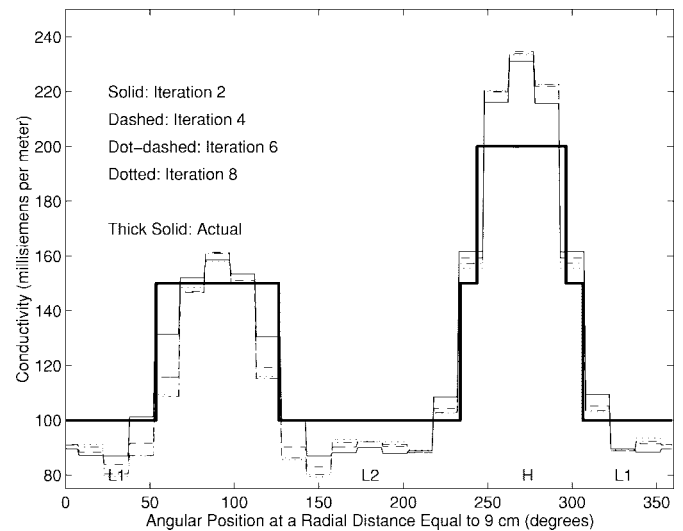


Fig. 11. Conductivity distribution as a function of angular position, calculated after several iterations of the CNRSER algorithm using separate real and quadrature voltage data generated from the geometry in Fig. 4. Marquardt regularization of the Jacobian matrix was implemented for these reconstructions.

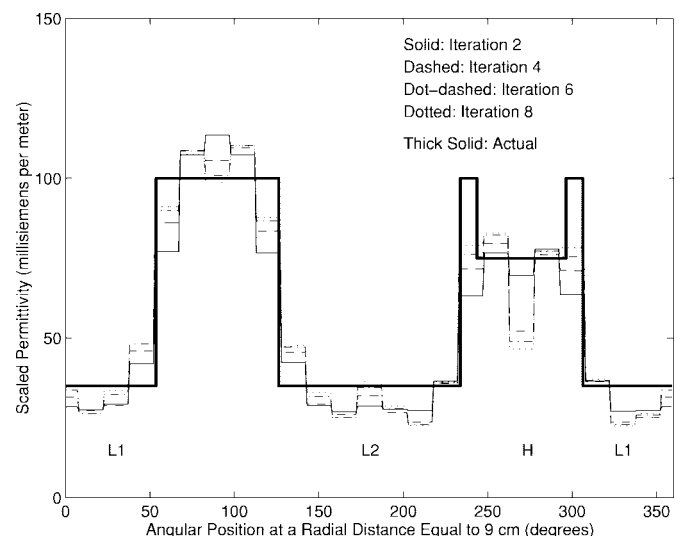


Fig. 12. Permittivity distribution as a function of angular position, calculated after several iterations of the CNRSER algorithm using separate real and quadrature voltage data generated from the geometry in Fig. 4. Marquardt regularization of the Jacobian matrix was implemented for these reconstructions.

algorithm. Marquardt regularization (gain equal to 0.2) was used for each of these reconstructions. The squared error between the real components of the measured and predicted voltages decreased by a factor of 4.47×10^3 after eight iterations while the squared error between the imaginary components of the measured and predicted voltages decreased by a factor of 2.85×10^2 .

Figs. 13 and 14 show reconstructions of the conductivity and permittivity distributions, respectively, of the simulated chest phantom, computed using gradient regularization of the Jacobian matrix. The gain of gradient term [Γ in (8)] was chosen to be 1.0. After four iterations of the CNRSER algorithm, the squared error between measured and predicted voltages was reduced by a factor of 79.8.

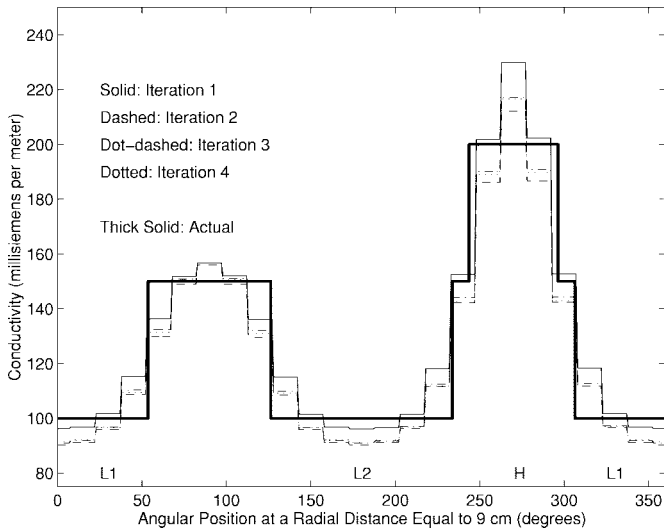


Fig. 13. Conductivity distribution as a function of angular position, calculated after four iterations of the CNRSER algorithm using complex voltage data generated from the geometry in Fig. 4. Gradient regularization of the Jacobian matrix was implemented for these reconstructions.

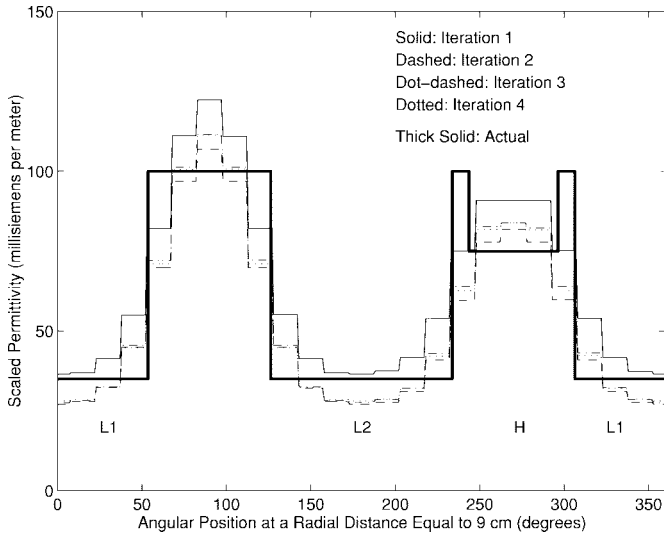


Fig. 14. Permittivity distribution as a function of angular position, calculated after four iterations of the CNRSER algorithm using complex voltage data generated from the geometry in Fig. 4. Gradient regularization of the Jacobian matrix was implemented for these reconstructions.

V. DISCUSSION

The results shown in the Section IV demonstrate two important characteristics of the CNRSER algorithm.

- 1) Reconstructions after multiple iterations of the CNRSER algorithm more closely resemble the true conductivity and permittivity distributions of B than the reconstructions given by only one step of the algorithm.
- 2) More accurate reconstructions of the conductivity and permittivity distributions result if these quantities are reconstructed simultaneously using complex voltage data measured on S .

Although the inverse admittivity problem is ill conditioned, it is possible to make better estimates of the reconstructed conductivity and permittivity distributions by executing a multistep algorithm, instead of considering only the linearized

problem. The ill-conditioned nature of the problem is a result of the characteristic that a large perturbation in the center of the body can result in minor perturbations in the voltages measured on the exterior of the body. As a result, the reconstructions are highly susceptible to noise.

The reconstructions displayed in Figs. 5 and 6 show that a linearized solution to the inverse problem results in an approximate estimate of the true conductivity and permittivity distributions. After the first iteration of the CNRSER algorithm, both the conductivity and permittivity distributions contain an inhomogeneity centered in the phantom. With more iterations, the values of conductivity and permittivity become more accurate, as seen in Figs. 5 and 6, respectively.

Accuracy of reconstructed data improves by computing the conductivity and permittivity distributions simultaneously using complex voltage data measured on S as input. The plots in Figs. 5 and 6, generated from reconstructions using complex voltages measured on S , more closely resemble the true distributions, after four iterations, than the plots in Figs. 7 and 8 which were generated from reconstructions which used real and quadrature components of the measured voltage on S separately. In fact, Figs. 7 and 8 show that updates to the conductivity and permittivity distributions actually progress in a direction opposite of the actual distributions toward the center of B . This was true even though the squared error between measured and predicted voltages for both the real and imaginary components of the boundary voltages on S decreased after each of four iterations.

Reconstructions of voltage data generated from the simulated chest phantom better represent the true conductivity and permittivity distributions in B when complex voltage is used as input to the algorithm. Figs. 9 and 10 show the conductivity and permittivity distributions, respectively, after several iterations of the CNRSER algorithm. By comparing these reconstructions to reconstructions of the conductivity (Fig. 11) and permittivity (Fig. 12) distributions computed using the real and quadrature components of the voltage on S separately, one can see significant differences, particularly in the conductivity distribution. Fig. 11 shows that the conductivity of the heart region (H) is overestimated while the conductivity near the edges of the lungs (L1 & L2) is underestimated after several iterations. These errors occur even though the squared error between measured and predicted voltages for the real and imaginary components of the boundary voltages on S decreased after each of eight iterations.

If the reconstructions in Figs. 9 and 10 are examined closely, one notices a general trend in the reconstructions of the conductivity and permittivity distributions: the reconstructions become less smooth as the CNRSER algorithm iterates. When experimental data is used as input to the CNRSER algorithm and Marquardt regularization is applied to the Jacobian matrix, this effect worsens. To force the reconstruction to be spatially smooth, the gradient term (β) was added to (8).

Figs. 13 and 14 show the conductivity and permittivity distributions calculated after four iterations of the CNRSER algorithm using complex voltage data as input. The gain of Γ in (8) was selected to be 1.0. It is evident that

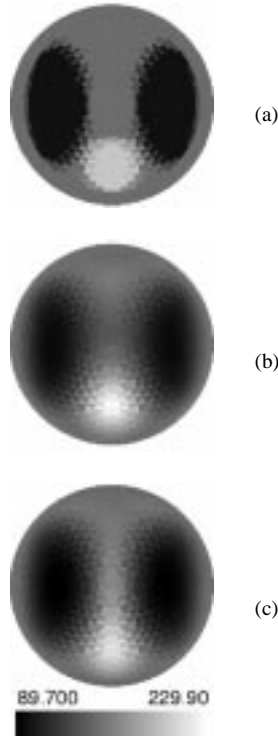


Fig. 15. (a) The ideal conductivity distribution and the reconstructed conductivity distribution, calculated after (b) the first and (c) the fourth iterations of the CNRSER algorithm using complex voltage data generated from the geometry in Fig. 4. Gradient regularization of the Jacobian matrix was implemented for these reconstructions. The ideal reconstruction was generated by computing the weighted-average of the conductivity values within a mesh element by the percentage of area containing the values. (Units are millisiemens per meter.)

the reconstructions in Figs. 13 and 14 are smoother when compared to the reconstructions in Figs. 9 and 10, respectively.

Fig. 15 shows the static reconstructions of the conductivity distribution after the first iteration [Fig. 15(b)] and after the fourth iteration [Fig. 15(c)] of the CNRSER algorithm using gradient regularization of the Jacobian matrix. From this figure, one can see that the reconstructed range and the resolution of the conductivity image are not adversely effected by this regularization method. Also included in Fig. 15 is an image of the ideal conductivity distribution [Fig. 15(a)]. This image was generated by computing a weighted-average of the conductivity values contained in a mesh element by the percentage of area containing the values. This image shows the best reconstruction that one would expect to compute given the boundaries of the objects in Fig. 4.

VI. CONCLUSION

The CNRSER algorithm solves the inverse admittivity problem using an iterative Newton-Raphson method. This algorithm is used in conjunction with a finite-element forward-solver that computes boundary voltages on a body, given the applied current vectors and the admittivity distribution within the body. By performing only a few iterations of the CNRSER algorithm, the estimates of the conductivity and permittivity distributions approach the true distributions in the examples presented. One is able to make better estimates of the true distributions if reconstruction algorithms are devised which

use complex voltage data, instead of operating on real and quadrature voltage data measured on S separately. The errors introduced in a linearized approach to the inverse problem are corrected as the number of iterations is increased.

APPENDIX

EXPRESSIONS FOR TERMS OF THE JACOBIAN MATRIX

There are four separate expressions for the components of the Jacobian matrix J defined in (16)

$$\begin{aligned} \frac{\partial F_{\rho_n}}{\partial \rho_m} = & 2 \sum_{k=1}^{L-1} \sum_{l=1}^L \left\{ U_{r,l}^k(\vec{\rho}) - V_{r,l}^k \right\} \frac{\partial^2 U_{r,l}^k(\vec{\rho})}{\partial \rho_n \partial \rho_m} \\ & + 2 \sum_{k=1}^{L-1} \sum_{l=1}^L \frac{\partial U_{r,l}^k(\vec{\rho})}{\partial \rho_n} \frac{\partial U_{r,l}^k(\vec{\rho})}{\partial \rho_m} \\ & + 2 \sum_{k=1}^{L-1} \sum_{l=1}^L \left\{ U_{q,l}^k(\vec{\rho}) - V_{q,l}^k \right\} \frac{\partial^2 U_{q,l}^k(\vec{\rho})}{\partial \rho_n \partial \rho_m} \\ & + 2 \sum_{k=1}^{L-1} \sum_{l=1}^L \frac{\partial U_{q,l}^k(\vec{\rho})}{\partial \rho_n} \frac{\partial U_{q,l}^k(\vec{\rho})}{\partial \rho_m} \\ & + 2\Gamma \int_B \nabla \frac{\partial \vec{\rho}}{\partial \rho_n} \cdot \nabla \frac{\partial \vec{\rho}}{\partial \rho_m} da \\ & + 2\Gamma \int_B \nabla \frac{\partial^2 \vec{\rho}}{\partial \rho_n \partial \rho_m} \cdot \nabla \vec{\rho} da \end{aligned} \quad (29)$$

$$\begin{aligned} \frac{\partial F_{q_n}}{\partial \rho_m} = & 2 \sum_{k=1}^{L-1} \sum_{l=1}^L \left\{ U_{r,l}^k(\vec{\rho}) - V_{r,l}^k \right\} \frac{\partial^2 U_{r,l}^k(\vec{\rho})}{\partial q_n \partial \rho_m} \\ & + 2 \sum_{k=1}^{L-1} \sum_{l=1}^L \frac{\partial U_{r,l}^k(\vec{\rho})}{\partial q_n} \frac{\partial U_{r,l}^k(\vec{\rho})}{\partial \rho_m} \\ & + 2 \sum_{k=1}^{L-1} \sum_{l=1}^L \left\{ U_{q,l}^k(\vec{\rho}) - V_{q,l}^k \right\} \frac{\partial^2 U_{q,l}^k(\vec{\rho})}{\partial q_n \partial \rho_m} \\ & + 2 \sum_{k=1}^{L-1} \sum_{l=1}^L \frac{\partial U_{q,l}^k(\vec{\rho})}{\partial q_n} \frac{\partial U_{q,l}^k(\vec{\rho})}{\partial \rho_m} \end{aligned} \quad (30)$$

$$\frac{\partial F_{\rho_n}}{\partial q_m} = \frac{\partial F_{q_m}}{\partial \rho_n} \quad (31)$$

$$\begin{aligned} \frac{\partial F_{q_n}}{\partial q_m} = & 2 \sum_{k=1}^{L-1} \sum_{l=1}^L \left\{ U_{r,l}^k(\vec{\rho}) - V_{r,l}^k \right\} \frac{\partial^2 U_{r,l}^k(\vec{\rho})}{\partial q_n \partial q_m} \\ & + 2 \sum_{k=1}^{L-1} \sum_{l=1}^L \frac{\partial U_{r,l}^k(\vec{\rho})}{\partial q_n} \frac{\partial U_{r,l}^k(\vec{\rho})}{\partial q_m} \\ & + 2 \sum_{k=1}^{L-1} \sum_{l=1}^L \left\{ U_{q,l}^k(\vec{\rho}) - V_{q,l}^k \right\} \frac{\partial^2 U_{q,l}^k(\vec{\rho})}{\partial q_n \partial q_m} \\ & + 2 \sum_{k=1}^{L-1} \sum_{l=1}^L \frac{\partial U_{q,l}^k(\vec{\rho})}{\partial q_n} \frac{\partial U_{q,l}^k(\vec{\rho})}{\partial q_m} \\ & + 2\Gamma \int_B \nabla \frac{\partial \vec{q}}{\partial q_n} \cdot \nabla \frac{\partial \vec{q}}{\partial q_m} da \\ & + 2\Gamma \int_B \nabla \frac{\partial^2 \vec{q}}{\partial q_n \partial q_m} \cdot \nabla \vec{q} da. \end{aligned} \quad (32)$$

REFERENCES

- [1] M. Cheney, D. Isaacson, J. C. Newell, S. Simske, and J. Goble, "NOSER: An algorithm for solving the inverse conductivity problem," *Int. J. Imag. Syst., Technol.*, pp. 66–75, 1990.
- [2] J. Sylvester and G. Uhlmann, "A uniqueness theorem for an inverse boundary value problem in electrical prospection," *Commun. Pure, Appl. Math.*, vol. 39, pp. 91–112, 1986.
- [3] D. C. Barber, B. H. Brown, and N. J. Avis, "Image reconstruction in electrical impedance tomography using filtered back projection," in *Proc. Annu. Int. Conf. IEEE Engineering in Medicine and Biology Society*, 1992, pp. 1691–1692.
- [4] B. H. Brown and A. D. Seagar, "The Sheffield data collection system," *Clin. Phys., Physiol. Meas.*, 8 suppl. A, pp. 91–97, 1987.
- [5] R. W. M. Smith, B. H. Brown, I. L. Freeston, F. J. McArdle, and D. Barber, "Real time electrical impedance imaging," in *Proc. Annu. Int. Conf. IEEE Engineering in Medicine and Biology Society*, 1990, pp. 104–105.
- [6] D. Isaacson and P. M. Edic, "An algorithm for impedance imaging," in *Proc. Annu. Int. Conf. IEEE Engineering in Medicine and Biology Society*, 1992, p. 1693.
- [7] P. M. Edic, G. J. Saulnier, J. C. Newell, and D. Isaacson, "A real-time electrical impedance tomograph," *IEEE Trans. Biomed. Eng.*, vol. 42, no. 9, pp. 849–859, Sept. 1995.
- [8] P. Hua, E. J. Woo, J. G. Webster, and W. J. Tompkins, "Iterative reconstruction methods using regularization and optimal current patterns in electrical impedance tomography," *IEEE Trans. Med. Imag.*, vol. 10, no. 4, pp. 621–628, Dec. 1991.
- [9] E. J. Woo, P. Hua, J. G. Webster, and W. J. Tompkins, "A robust image reconstruction algorithm and its parallel implementation in electrical impedance tomography," *IEEE Trans. Med. Imag.*, vol. 12, no. 2, pp. 137–146, June 1993.
- [10] T. J. Yorkey, J. G. Webster, and W. J. Tompkins, "Comparing reconstruction algorithms for electrical impedance tomography," *IEEE Trans. Biomed. Eng.*, vol. BME-34, no. 11, pp. 843–852, Nov. 1987.
- [11] M. R. Eggeleston, R. J. Schwabe, L. F. Coffin, and D. Isaacson, "The application of electric current computed tomography to defect imaging in metals," *Rev. Quantitat. Nondestructive Evaluation*, vol. 9A, pp. 455–462, 1990.
- [12] D. Isaacson, "Distinguishability of conductivities by electric current computed tomography," *IEEE Trans. Med. Imag.*, vol. M1-5, pp. 91–95, 1986.
- [13] M. Cheney and D. Isaacson, "Distinguishability in impedance imaging," *IEEE Trans. Biomed. Eng.*, vol. 39, no. 8, pp. 852–860, Aug. 1992.
- [14] W. H. Press, Ed., *Numerical Recipes in C: The Art of Scientific Computing*. New York: Cambridge Univ. Press, 1992.
- [15] E. Isaacson and H. B. Keller, Eds., *Analysis of Numerical Methods*. New York: Wiley, 1966.
- [16] K.-S. Cheng, D. Isaacson, J. C. Newell, and D. G. Gisser, "Electrode models for electric current computed tomography," *IEEE Trans. Biomed. Eng.*, vol. 36, pp. 918–924, 1989.
- [17] E. Somersalo, M. Cheney, and D. Isaacson, "Existence and uniqueness of electrode models for electric current computed tomography," *SIAM J. Appl. Math.*, vol. 52, no. 4, pp. 1023–1040, Aug. 1992.
- [18] M. Pidcock, S. Ciulli, and S. Ispas, "Singularities of mixed boundary value problems in electrical impedance tomography," *Physiol. Meas.*, vol. 16, no. 3, suppl. A, pp. A213–218, Aug. 1995.
- [19] H. P. Schwan and C. F. Kay, "The conductivity of living tissue," *Ann. NYAS*, vol. 65, pp. 1007–1013, 1957.



Peter M. Edic (S'93–M'95) was born in Utica, NY, on December 25, 1959. He received the A.A.S. degree in electrical engineering technology from Mohawk Valley Community College, Utica, NY, in 1987, the B.S. degree in electrical engineering from Syracuse University, Syracuse, NY, in 1990, and the M.S. and Ph.D. degrees in electrical engineering from Rensselaer Polytechnic Institute, Troy, NY, in 1991 and 1994, respectively.

He is currently working at the General Electric Corporate Research and Development Center, Schenectady, NY. His research interests include signal/image processing, medical imaging, data visualization, and microprocessor-based medical instrumentation.

David Isaacson (M'86) received the Ph.D. degree in mathematics from New York University's Courant Institute of Mathematical Sciences, New York, in 1976.

He is a Professor of Mathematics at Rensselaer Polytechnic Institute, Troy, NY. He is currently working on problems arising in the use of electromagnetic fields for the diagnosis and treatment of disease.

Gary J. Saulnier (S'80–M'84–SM'95) was born in Fall River, MA. He received the B.S., M.E., and Ph.D. degrees in electrical engineering from Rensselaer Polytechnic Institute, Troy, NY, in 1980, 1982, and 1985, respectively.

In 1984, he joined General Electric Corporate Research and Development Center, Schenectady, NY, where he studied the design and implementation of bandwidth-efficient digital modulation techniques for fading channels. Since 1986, he has been on the faculty of the Electrical, Computer and Systems Engineering Department at Rensselaer Polytechnic Institute where he is currently an Associate Professor. His research interests include modems for mobile and mobile-satellite channels, antijam spread spectrum systems, and electronic instrumentation for biomedical applications.

Hemant Jain was born in Meerut, India, on January 3, 1973. He received the B.Tech. degree in electrical engineering from Indian Institute of Technology, Kanpur, India, in 1993, and M.S. and Ph.D. degrees in biomedical engineering from Rensselaer Polytechnic Institute, Troy, NY, in 1996 and 1997, respectively.

He is currently working at Epic Systems Corporation, Madison, WI. His main research interests include noninvasive imaging techniques and high performance computing for biomedical applications.



Jonathan C. Newell (S'64–M'69) received the B.S. and M.S. degrees in electrical engineering from Rensselaer Polytechnic Institute, Troy, NY, where he graduated in 1968, and the Ph.D. degree in physiology from Albany Medical College, Albany, NY, in 1974.

He is now Professor of Biomedical Engineering at Rensselaer Polytechnic Institute and Professor of Physiology and Surgery at Albany Medical College. His research interests have included the regulation of the pulmonary circulation in hypoxia, and pulmonary gas exchange in injured patients with acute respiratory failure. His recent work has been the development of an adaptive system for electrical impedance imaging.